

Same Signal, Different Story: Demystifying Receiver Effects in Wi-Fi Channel State Information

Fabian Portner, Francesco Gringoli, Matthias Hollick, and Arash Asadi

Abstract—Wi-Fi sensing has emerged as a versatile tool for tasks such as localization, gesture recognition, and vital-sign monitoring, enabling applications from smart environments to personalized healthcare. However, sensing accuracy often significantly degrades when pretrained models are deployed across different commodity receivers. We present the first systematic comparison of Channel State Information (CSI) across diverse Commercial Off-The-Shelf Wi-Fi sensing platforms. Using a unified experimental setup delivering precisely precoded signals simultaneously to multiple receivers, we isolate receiver-specific variability. We find that dominant cross-device differences arise from Automatic Gain Control and consistent subcarrier nonlinearities. We propose a simple gain-alignment preprocessing step, recovering most of the lost accuracy (up to 75%) in cross-device Human Activity Recognition model deployments. Without preprocessing, model accuracy sharply drops—effectively breaking practical deployments. Additional analyses reveal measurable inherent differences in receiver faithfulness, sensitivity and noise. While these receiver-induced differences do not significantly affect robust sensing tasks such as Human Activity Recognition, they become relevant in scenarios demanding high precision (e.g., single-shot time of flight). Our findings demonstrate that cross-device variability in CSI is real but manageable, and we provide tools and guidelines for robust, hardware-agnostic Wi-Fi sensing.

I. INTRODUCTION

Wi-Fi Channel State Information (CSI) has evolved from a communication by-product into a sensing enabler that now powers tasks such as localization, gesture recognition, and even vital-sign monitoring. However, a critical obstacle to robust and portable sensing (that is, the ability to apply sensing models across different hardware platforms) has received limited systematic attention: **commodity receivers distort CSI in device-specific ways that degrade generalization across devices**. Differences in hardware, firmware, and signal processing pipelines, even within identical device families, cause receivers to perceive the wireless channel differently. As a result, sensing models trained on one device often fail on others, and seemingly minor discrepancies across studies may reflect hardware quirks rather than algorithmic differences. Despite the growing importance of CSI, the community lacks a clear understanding of how receiver-induced variability manifests and impacts downstream tasks.

Unlike communication systems, which rely on equalization to abstract away channel effects, CSI-based applications

require a stable, interpretable relationship between the environment and the reported CSI. However, various receiver components, including the front-end, Automatic Gain Control (AGC), CSI estimation pipeline, and lack of synchronization, can introduce nontrivial yet often deterministic distortions, as well as differences in sensitivity and noise levels.

These effects challenge the design of portable sensing systems. In sensing, they limit model transfer. In fingerprinting, they yield device-specific signatures. In security, they introduce inconsistencies that weaken authentication. Yet no standardized methodology exists for evaluating or mitigating these differences, and many systems remain tightly coupled to specific devices.

Some effects, mainly concerning phase noise, have long been investigated and can either be corrected for or circumvented [1]–[12]. Some works have gone further and investigated static, nonlinear receiver-induced distortions in CSI, such as subcarrier-dependent amplitude and phase artifacts [13]–[15], and shown that these effects are repeatable and thus calibratable. However, these studies examine only a narrow set of devices and provide limited insight into how such distortions manifest across platforms or affect downstream performance more broadly.

We address this gap by jointly studying receiver effects in CSI and deep learning-based sensing models through a systematic black-box comparison across Commercial Off-The-Shelf (COTS) platforms. Using a unified experimental setup that delivers identical, precisely precoded signals to multiple receivers, we isolate and quantify receiver-induced differences. We enhance existing CSI extraction tools [13], [16], [17] to support heterogeneous Network Interface Cards (NICs), enabling direct comparison of correctable distortions and inherent hardware differences.

In order to assess practical consequences, we evaluate three representative tasks: Doppler-based velocity estimation, time of flight (ToF) extraction from Power Delay Profile (PDP), and deep learning-based Human Activity Recognition (HAR). We find that most cross-device differences stem from predictable effects, namely AGC behavior and subcarrier nonlinearities, which can be corrected using a lightweight gain-alignment step. After correction, residual differences in sensitivity and noise remain, but have limited impact on robust sensing tasks, becoming relevant only in precision-critical settings such as single-shot ToF. Our findings offer practical guidance and tools for building portable, hardware-agnostic Wi-Fi sensing systems.

Fabian Portner and Arash Asadi are with Delft University of Technology, Delft, The Netherlands (email: fportner@tudelft.nl; aasadi@tudelft.nl).

Francesco Gringoli is with the University of Brescia, Brescia, Italy (email: francesco.gringoli@unibs.it).

Matthias Hollick is with the Technical University of Darmstadt, Darmstadt, Germany (email: matthias.hollick@seemoo.tu-darmstadt.de).

A. Contributions

Our contributions are as follows:

- We design a unified experimental setup that delivers identical precoded signals to multiple receivers simultaneously, enabling controlled black-box comparison without ground truth, and release all collection and processing code as open source.
- We systematically evaluate CSI quality across all major COTS Wi-Fi platforms, including *Intel IWL5300*, *Intel AX210*, *Qualcomm Atheros QCA*, *Broadcom*, *Espressif ESP32*, and a *USRP x310*, and publicly release the collected CSI and derived data.
- We identify that most cross-device differences stem from predictable receiver-induced distortions, including consistent nonlinear subcarrier shapes and AGC behavior, which can be effectively corrected.
- We propose a simple gain removal with feature-wise standardization that outperforms alternative schemes and recovers up to 75% of the cross-device accuracy loss for several HAR models.
- We further quantify residual differences in noise, faithfulness, and sensitivity, showing that while measurable, these have limited impact on practical tasks such as HAR and Doppler-based velocity estimation.

II. BACKGROUND

A. Channel State Information

The wireless channel between a transmitter and receiver varies as people move, objects reflect, and paths change. To ensure reliable communication, receivers repeatedly estimate the channel state and compensate for its variations.

Wi-Fi employs Orthogonal Frequency Division Multiplexing (OFDM), dividing the communication bandwidth into multiple narrowband subcarriers. Within the duration of a single packet, the channel is typically assumed linear and time-invariant. Under this assumption, the received OFDM symbol on subcarrier k can be expressed simply as

$$R_k = H_k S_k, \quad (1)$$

where S_k denotes the transmitted symbol, R_k the received symbol, and H_k the Channel Frequency Response (CFR). In multipath environments, H_k decomposes into a sum of P propagation paths [18]:

$$H_k = \sum_{p=1}^P \alpha_{p,k} \exp(-j2\pi f_k \tau_p),$$

where $\alpha_{p,k}$ and τ_p represent the attenuation and delay of the p -th path, and f_k is the frequency of subcarrier k . Over multiple packet transmissions, these path parameters evolve slowly, causing H_k to vary.

Receivers estimate the channel from fixed training symbols in the physical-layer preamble, as defined in the 802.11 standard, yielding per-packet CSI vectors $\hat{H}[n] = [\hat{H}_1[n], \dots, \hat{H}_K[n]]$. Ideally, these estimates match the true channel up to a constant scaling factor ($\hat{H}[n] = cH[n]$). In practice, COTS receivers introduce distortions due to gain

control, synchronization offsets, and hardware nonlinearities, which we model as a receiver-specific transformation $\hat{H}[n] = E(H[n])$. For each subcarrier, we decompose E into amplitude and phase distortions:

$$\hat{H}_k[n] = \beta_k[n] \exp(-j2\pi\phi_k[n]) H_k[n] + \eta_k[n],$$

where $\beta_k[n]$ represents amplitude effects, $\phi_k[n]$ phase distortions, and $\eta_k[n]$ additive noise. For tractability, $\beta_k[n]$ and $\phi_k[n]$ are typically modeled explicitly. Phase distortions are often taken to be linear in subcarrier index k due to Sampling Time Offset (STO), Carrier Frequency Offset (CFO), and Cyclic Shift Diversity (CSD) [14], [19], while gain control is approximated as a global amplitude factor across subcarriers.

Real-world receivers, however, exhibit additional artifacts, including nonlinear subcarrier responses and chipset-specific quirks, that violate these assumptions. Prior work [14], [15] shows that such nonlinearities are static and repeatable, enabling calibration. To explicitly include them, we model

$$\begin{aligned} \beta_k[n] &= G[n] \cdot A_k, \\ \phi_k[n] &= a[n] \cdot k + b[n] + \Phi_k, \end{aligned} \quad (2)$$

where amplitudes factor into a global gain $G[n]$ and subcarrier profile A_k , and phases into a linear trend plus static offset Φ_k . This formulation captures dominant receiver-side distortions.

B. Related Work

a) *CSI Extraction on Commodity Devices*: A growing body of tools enables CSI collection on commodity Wi-Fi hardware. The pioneering Intel 5300 CSI Tool [16] introduced modified firmware and drivers to obtain CSI from 802.11n NICs. Subsequent platforms expanded CSI access: the Atheros CSI tool [13] targeted Qualcomm Atheros NICs, the Nexmon framework [20] provided extraction for Broadcom 802.11ac chips, Espressif's *ESP32* Wi-Fi module [17] made low-cost boards popular, and the PicoScenes platform [15] unified support for Intel, Atheros, and Software-Defined Radio (SDR) devices with additional capabilities. These tools have opened CSI research to a variety of devices, but each receiver's CSI may embody unique quirks. Our work complements this landscape with a side-by-side, cross-device analysis of CSI from multiple COTS receivers using a common transmitter to pinpoint receiver-induced distortions.

b) *Receiver-Induced Distortions*: Previous studies have highlighted that CSI measurements suffer from hardware-induced nonlinearities varying across chipsets. Zhuo et al. [21] observed nonlinear distortions they attributed to IQ imbalance, later introducing π -Splicer [14] to correct them. Jiang et al. [15] re-examined those distortions, attributing them to baseband filter artifacts, and comparing across Intel IWL5300 and Atheros NICs. Chi et al. [7] applied a simple cable-based calibration to eliminate these distortions, assuming temporal consistency.

However, these prior studies each examined a limited set of devices and the origin of nonlinear distortions, whereas our work provides a broader, side-by-side comparison across diverse receivers and evaluates the practical impact of such distortions on sensing applications.

III. SETUP AND METHODOLOGY

To characterize receiver-dependent effects, we must isolate them from the variability of wireless channels. In over-the-air (OTA) scenarios, fluctuating channel conditions and transmitter-induced effects make CSI difficult to interpret because no channel ground truth is available. We therefore build a controlled testbed and introduce a precoding methodology that emulates known, time-varying channel changes.

We leverage a high-fidelity SDR as our transmitter, which minimizes TX-induced variability and enables precise control over the transmitted Wi-Fi frames. By routing the signal over cable and distributing an identical input to all receivers via a low-noise power splitter, we eliminate wireless channel variability and can directly compare how different receivers respond to deliberate, controlled channel modifications.

A. Experimental Setup

To compare CSI across multiple receivers, the experimental setup includes eight devices spanning six distinct receiver models with descriptive names used in the rest of the paper:

- **2×ASUS RT-AC86U** routers named *asus1* and *asus2*
- **2×ESP32-S3** microcontrollers named *ESP1* and *ESP2*
- **1×Intel AX210** NIC named *ax210*
- **1×Intel IWL5300** NIC named *iwl5300*
- **1×USRP N2954-R** SDR named *x310*
- **1×Qualcomm Atheros QCA AR9462** named *qca*

To assess intra-family variability, we duplicate the least and most constrained COTS devices: the high-end *ASUS* RT-AC86U and the low-cost *ESP32*. We observe minor but consistent differences between such devices (see Section IV), indicating that receiver-induced effects can arise even within a single hardware family. To limit setup complexity, we restrict duplication to these two representative cases and leave a more exhaustive intra-family analysis for future work.

The Intel cards and *x310* are operated by an *Experiment Host PC* running Ubuntu 22.04, and configured via PicoScenes [15]. The ESPs are attached to the same host and use a custom-developed extractor for scripted CSI collection, while CSI from the *ASUS* routers is obtained via a Nexmon-based custom extractor [20]. A second PC running Ubuntu 24.04 operates the *qca* independently to avoid driver conflicts with PicoScenes¹, and we extract CSI using a ported version of the Atheros CSI tool [13] compatible with newer kernels.

For the transmitter, another PC operates a *second* USRP N2954-R. We use MATLAB, specifically the WLAN Toolbox, to generate IQ samples corresponding to 802.11n Wi-Fi frames. The transmitter connects via cable to a waveguide power splitter (ZN8PD1-63W-S+), which distributes the same signal to all eight receivers. A schematic overview of our setup is presented in Figure 1.

The *iwl5300* and Atheros CSI tools are incompatible for collecting CSI from the same frames: the former reports CSI only for frames addressed to a hardcoded MAC address, while the latter requires frames addressed to its hardware MAC

¹PicoScenes officially features Atheros devices, but this is currently disabled due to Issue 197.

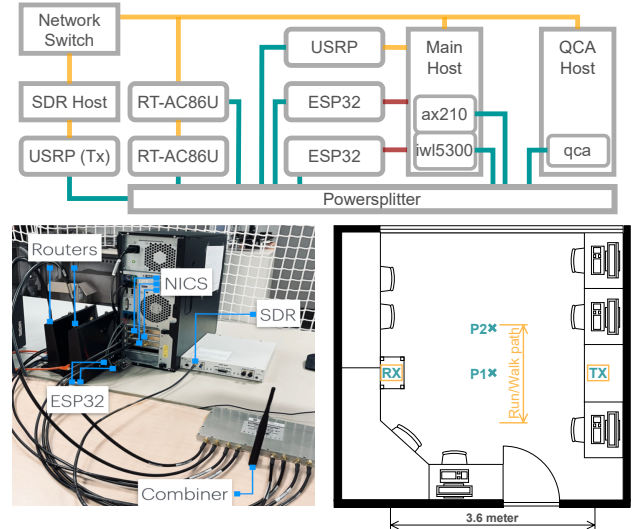


Figure 1. Experimental setup. Top: schematic representation with RF connections in cyan, ethernet in yellow, USB in red. Bottom: photograph of the physical setup and corresponding floorplan with HAR person positions.

address. We therefore send interleaved frames that differ only in the destination MAC address. The other extractors have no such restriction; for them we simply filter frames addressed to the *iwl5300*.

We conduct all experiments using single-antenna configurations and a channel bandwidth of 20 MHz, as imposed by the ESPs, which operate only on 20 MHz in the 2.4 GHz band and have a single antenna. All devices operate passively in monitor mode, without association to an access point.

To ensure uniform analysis, we transform CSI from all devices into a common format and store it in Apache Parquet files. The Experiment Host coordinates all devices over a local network for synchronized operation and centralized data collection, and the pipeline is scripted to detect and recover from common runtime errors.

B. OFDM Precoding

In OTA experiments, assessing CSI accuracy is difficult because no channel ground truth is available. We therefore exploit the fact that the transmitted OFDM symbols x_k are fixed by the 802.11 standard and introduce controlled modifications via precoding. Using the MATLAB WLAN Toolbox, we generate Wi-Fi 802.11n frames and precode all symbols in a packet with subcarrier-specific complex scaling factors $c_k \in \mathbb{C}$, yielding $x'_k = c_k x_k$. From the receiver's perspective, this is indistinguishable from a change in the channel, and the received signal becomes $y = H \odot c \odot x$, where H is the true channel and \odot denotes the Hadamard product.

Because the receiver does not know c , it effectively estimates $\hat{H} = E(H \odot c)$. If the channel remains constant, c appears as a consistent, relative change in \hat{H} , providing a stable reference to assess how closely the estimates follow the expected changes and how much distortion the internal estimation pipeline E introduces. By precisely controlling c_k while keeping all other conditions fixed, we isolate the behavior of E and systematically evaluate how each receiver responds to small, deliberate input changes: its sensitivity, added noise, and temporal consistency.

IV. CROSS-RECEIVER SENSING

We study how receiver hardware affects performance and portability in Wi-Fi sensing by measuring gaps in HAR and Doppler tasks and showing that simple preprocessing largely restores generalization across heterogeneous receivers.

A. Impact of different receivers

We first ask whether hardware differences meaningfully affect sensing tasks such as HAR. To address this, we use ARIL [22], an open-source HAR model with a ResNet backbone, and test it on data from different receivers to evaluate device-dependent sensitivities in a neural-network application. We follow the authors’ published training procedure¹, but backpropagate only an activity-classification loss (ignoring the location head). Because HAR requires human motion in an actual propagation environment, we replace the transmitter–power splitter cable with a TX/RX antenna pair.

Dataset and protocol: A single participant provided informed consent and performed seven activities facing the RX (jumping, standing still, walking, running, squat, clapping, and waving arms) plus an empty-room baseline. The participant stood in either LOS or NLOS (Figure 1), yielding 90 repetitions per activity across conditions. We record at 500 fps for 3 s and subsample each series to 700 frames of 56 subcarriers to mitigate packet-loss inhomogeneity. We focus on receiver variability: in one office setup, we vary LOS/NLOS positions and repeat trials, while all receivers see the same channel realizations via the power splitter. This suffices for our purpose, since we use HAR to probe task-relevant information exposure per device, not to benchmark HAR in general. As in the original implementation, we do not apply data standardization.

We evaluate model performance using **stratified 5-fold CV repeated 20 times** (100 train/test splits per receiver). Repeated k -fold CV is recommended for small–moderate datasets as a low-bias, lower-variance estimator [23]–[25]. We report mean accuracy and its standard deviation across splits.

Results: Figure 2 reveals that (*qca*, *iwl5300*, *ASUS*) consistently achieve accuracies around 95%, whereas the two *ESP32* modules lag by about 2–4%. Interestingly, *ESP1* underperforms *ESP2*, despite nominally identical specification, suggesting hardware variability within the *ESP32* family that could merit further investigation in future work.

Key takeaway: While all devices enable ARIL to achieve high accuracy, hardware differences between receivers meaningfully affect classification performance. Employing a low-bias estimator such as repeated stratified CV is essential for quantifying these effects and comparing improvements in Wi-Fi sensing pipelines.

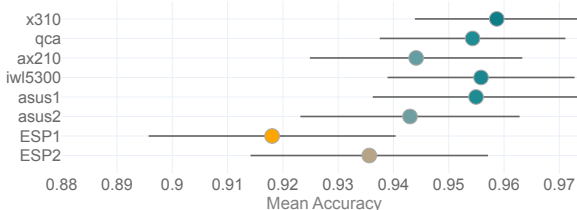


Figure 2. Per-receiver accuracy ± 1 SD, estimated with 20×5 -fold CV.

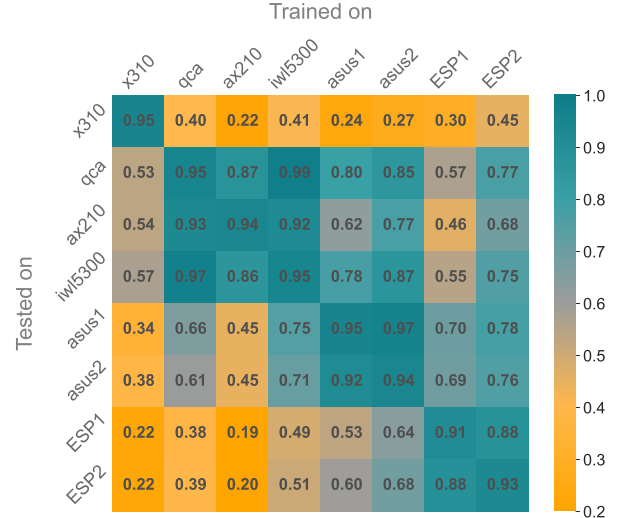


Figure 3. Confusion matrices when ARIL is trained on one receiver (rows) and tested on others (columns), without normalization.

B. When the receiver changes: cross-device generalization

Retraining models for every receiver does not scale: labeling new data is costly, training adds overhead, and both steps hinder deployment at scale. As Wi-Fi sensing moves toward broader use, reusing pretrained models across devices becomes a *practical necessity*. Yet while cross-environment transfer has been studied, the role of the receiver itself has gone largely unexamined.

Cross-device evaluation: We now ask whether a model trained on one receiver transfers to others. Because different devices report CSI on very different amplitude scales, we add a single feature-wise z-score standardization step, separately for each receiver and for the train and test sets; all other hyperparameters and training choices remain identical to the original ARIL implementation. When training and testing on the same receiver, we keep an 80/20 train–test split. For cross-device transfer, we instead train ARIL on all data from one device and test on all samples from another, so these evaluations benefit from a slightly larger training set; Figure 3 shows the resulting confusion matrices. Performance drops significantly when classifying on data from a different receiver. The most severe degradation occurs when training on *x310*: although it performs well on its own data, accuracy drops below 60% on every other device, reaching as low as 20% on *ESP1*. *qca*, *ax210* and *iwl5300* exhibit good transfer accuracies, likely aided by the increased training data. The two ESPs generalize well across each other, with only a slight 3% – 5% accuracy reduction, but model performance breaks across device families.

C. A likely cause: AGC

HAR works by recognizing patterns of relative CSI change over the activity duration. A well-known confounder over time is AGC, which dynamically rescales CSI amplitudes based on received signal strength. This introduces an unknown scaling effect that obscures amplitude variations. Without a

¹ARIL GitHub repository.

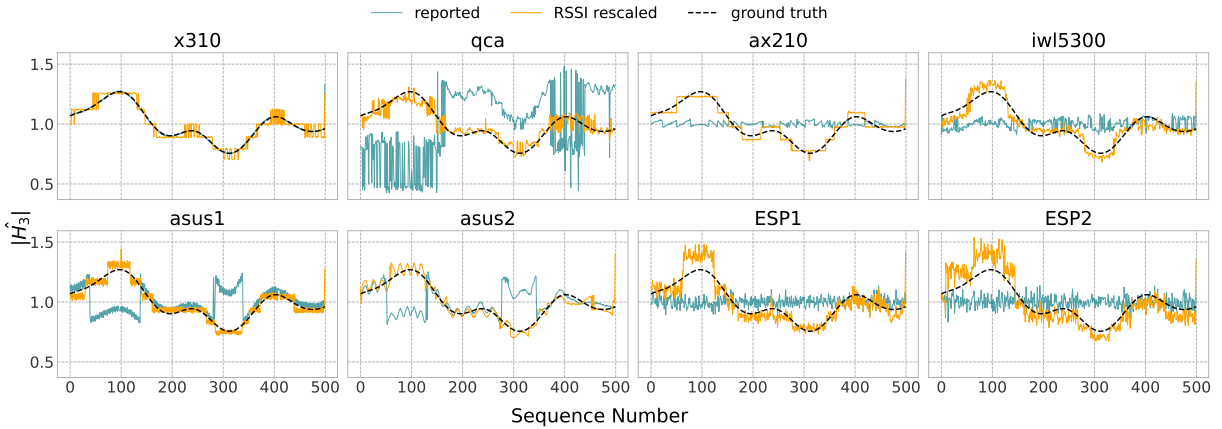


Figure 4. Reported CSI amplitudes of subcarrier $k = 3$ per receiver, normalized to series mean, versus ground truth scaling curve.

gain indicator, it is challenging to distinguish channel-induced changes from AGC artifacts, hindering applications that rely on accurate amplitude information. Because amplitude directly influences downstream tasks (e.g., Doppler extraction), CSI-based applications should preserve its natural variation.

One practical mitigation is to rescale CSI amplitudes using Received Signal Strength Indicator (RSSI) via the factor [26]

$$s = \sqrt{\frac{10^{RSS/10}}{\sum_k |\hat{H}_k|^2}}. \quad (3)$$

However, RSSI is a coarse metric with much lower resolution than CSI, limiting its effectiveness.

To investigate gain control across devices, we again connect the transmitter and power splitter by cable and apply a common amplitude precoding factor across all subcarriers (see Section III-B), varying transmit gain smoothly over time. In an ideal scenario without AGC, a single global normalization would let each subcarrier amplitude follow the expected curve.

Figure 4 shows CSI amplitude for subcarrier $k = 3$ before and after Equation (3). The results reveal stark differences in how gain control affects various devices. The *x310* (no AGC) accurately preserves the original variations; the measured curve shadows the ground truth. In contrast, *ASUS* devices exhibit large, infrequent step changes, making gain control effects easy to spot. Intel devices also show step-like adjustments, albeit smaller and more frequent, making them harder to discern visually. For *ESP32* and *QCA* devices, the impact of gain control is indistinguishable from noise; its application appears almost random, completely obscuring the underlying pattern to the human eye.

While RSSI rescaling moves amplitudes toward the expected curves, it still leaves substantial device-to-device variation because RSSI is itself receiver-dependent.

D. No gain, no pain

To address this, we propose to simply remove large-scale gain by a simple, yet effective normalization

$$\hat{H}_k^N = \frac{\hat{H}_k}{\frac{1}{K} \sum_k |\hat{H}_k|}. \quad (4)$$

The impact of this transformation on the information content can be stated precisely by investigating the Fisher information [27]. Under a differentiable transformation $\mathbf{y} = g(\mathbf{h})$, the Fisher information matrix becomes $\mathcal{I}_g = J \mathcal{I} J^\top$, where $J = I - \frac{1}{K} \mathbf{1} \mathbf{1}^\top$ is the Jacobian of the normalization. This projection removes the component along the constant-gain direction. The rank of the Fisher information consequently drops by (just) one $\text{rank}(\mathcal{I}_g) = \text{rank}(\mathcal{I}) - 1$. Contrary to some prior claims [1], this discards not all amplitude information but a single scalar: the large-scale gain *shared across all subcarriers*. However, motion and environmental changes can affect large-scale gain, so this transformation may still suppress signal the network could otherwise exploit. The question is *whether the remaining dimensions, those orthogonal to global gain, still contain enough information for accurate sensing*.

Retraining and outcome: To test this, we retrain ARIL on the normalized data under the setup presented in Section IV-B. For each receiver, we quantify uncertainty in the mean accuracy via nonparametric bootstrapping: we draw 10 000 resamples (with replacement) of the $K = 100$ CV folds, compute the mean accuracy for each resample, and report the 0.5–99.5 bias-corrected and accelerated (BCa) percentile limits [28], which adjust for median bias and skew. These intervals indicate whether the observed changes in mean accuracy are compatible with random variation. As shown in Figure 5, performance is mostly maintained or improved. The *ESP32* devices and *asus1* benefit most, likely due to stabilization of erratic gain behavior, whereas the *x310* exhibits a small drop, indicating that without AGC, absolute gain carried some useful signal.

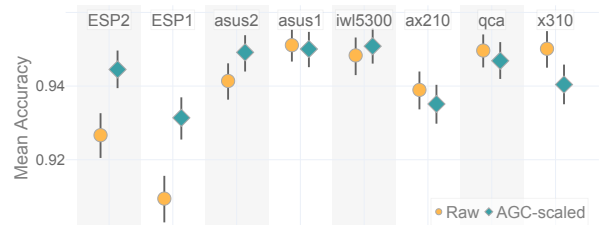


Figure 5. Per-receiver mean accuracy before/after ℓ_1 normalization. Error bars: 99% BCa bootstrap CIs from 10 000 resamples of the $K = 100$ CV folds.



Figure 6. Confusion matrices after ℓ_1 normalization, showing markedly improved cross-device generalization.

Cross-device generalization improves: Figure 6 shows updated confusion matrices. Normalization yields a substantial boost in cross-device performance: all off-diagonal accuracies now exceed 82%, most exceeding 95% and some nearing 99%. A simple rescaling step effectively restores generalization in a way that preserves performance across all devices. We note that nonlinearity equalization did not yield any notable improvement, indicating that learned features rely more on relative changes over time. This shows that the shift in distribution between different receivers is mainly due to AGC.

Outlook: Normalization resolves much of the observed divergence, but not all. Worst-case, accuracy still drops by up to 10 - 15%. For industrial deployments with controlled hardware variation, this may be acceptable. But in scenarios involving heterogeneous receivers or crowdsourced datasets, additional techniques, such as multi-device training or fine-tuning, may be necessary to ensure full portability.

E. Alternative gain preprocessing methods

We now evaluate ℓ_1 normalization (Equation (4)) against alternative preprocessing strategies proposed to mitigate AGC-induced distortions in CSI.

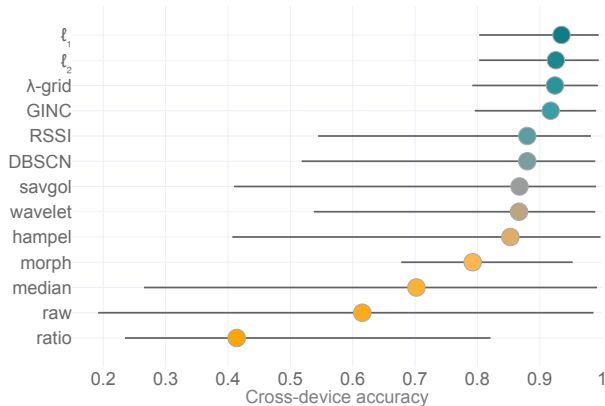


Figure 7. Cross-device performance under different preprocessing strategies; Markers show median, whiskers worst-case accuracies across all devices.

We cover three categories: (i) methods that discard large-scale gain, including ℓ_2 normalization [29], gain-invariant features (morphological [30] and double-ratios [11]); (ii) explicit gain-recovery methods, which attempt to recover a consistent amplitude scale despite AGC, including RSSI-based amplitude rescaling (Equation (3)), DBSCAN clustering [31], and two maximum-likelihood algorithms by Ratnam et al. [1]—GINC (Alg. 1), and λ -grid (Alg. 2); and (iii) smoothing filters to suppress AGC fluctuations: median [32], Savitzky–Golay [33], wavelet [34], and Hampel [34].

Results: Figure 7 shows ℓ_1 normalization outperforming all alternatives, with median cross-device accuracy above 90%. Explicit gain-recovery methods are competitive, trailing slightly in both median and worst-case accuracy. Smoothing-based methods drop to 85-89% median and struggle in worst-case stability. Morphological features, median filtering, and raw CSI each stay below 80% median. Double-ratio features perform worst overall, at $\approx 40\%$, below raw data.

Take-away: Explicit gain-recovery offers no meaningful accuracy advantage despite higher computational cost. A simple, carefully chosen normalization—our proposed ℓ_1 procedure—consistently yields the highest cross-device accuracy, superior robustness, and far lower compute.

F. Standardization ablation

We now ablate classic standardization schemes that might compensate for AGC-induced scale differences. We combine min-max and z-score standardization with four scopes: (i) *global*, a single transform over all CSI values; (ii) *window*, one transform per example; (iii) *subcarrier*, one transform per subcarrier, pooling all times and examples; and (iv) *examples*, one transform per time-frequency bin across examples (feature-wise standardization).

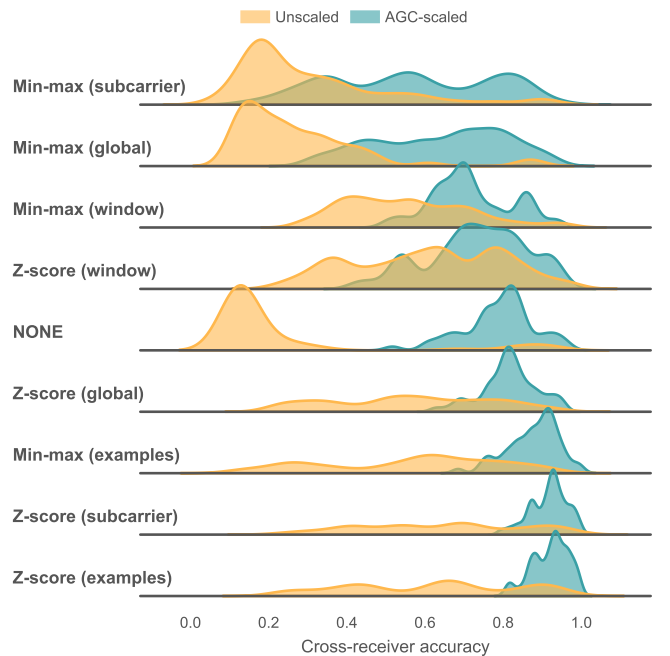


Figure 8. Distributions of cross-device accuracies under different standardization strategies, with and without gain normalization. Curves aggregate off-diagonal accuracies across all train-test device pairs.

Results: Figure 8 shows the resulting distributions of cross-device accuracies. Standardization clearly matters: example-wise standardization across examples (scope (iv)) gives the strongest cross-device performance, indicating that within-example amplitude changes carry useful information. Global, window, and subcarrier scopes provide smaller or inconsistent gains. Across all variants, gain-normalized inputs give better cross-device performance: accuracies are higher on average, and severe failures on particular train–test receiver pairs become much less common.

Take-away: Standardization improves cross-device robustness, but it does not replace gain normalization. The best results arise from combining example-wise standardization with our gain normalization, which together deliver the highest and most stable accuracies across receivers.

G. Generality across HAR architectures

So far we have focused on ARIL. To test whether the same cross-device effects appear in other HAR architectures, we also evaluate WiADN [35], a recurrent Conformer [36], and RGANet [37]. We follow the public code with only minimal changes required by our activity-only, 700-sample setting: WiADN is run with activity loss only and a patched attention-mask generator that supports 700-sample windows; the recurrent Conformer uses its UT-HAR configuration unchanged; and RGANet uses the released UT_HAR_GRU_Attention and UT-HAR code path. We prepend the same feature-wise z-score standardization as in Section IV-B with no other architectural or hyperparameter changes.

Results: Figure 9 shows the resulting cross-device accuracy distributions. All four models suffer from clear cross-receiver degradation without gain normalization, despite standardization. After applying gain normalization, the distributions shift to higher accuracies for every architecture, and low-accuracy cases become rare.

Take-away: Cross-device sensitivity is not specific to ARIL: it appears across convolutional, recurrent, and attention-based HAR models. Gain normalization, combined with simple feature-wise standardization, consistently improves cross-receiver compatibility for all architectures we test.

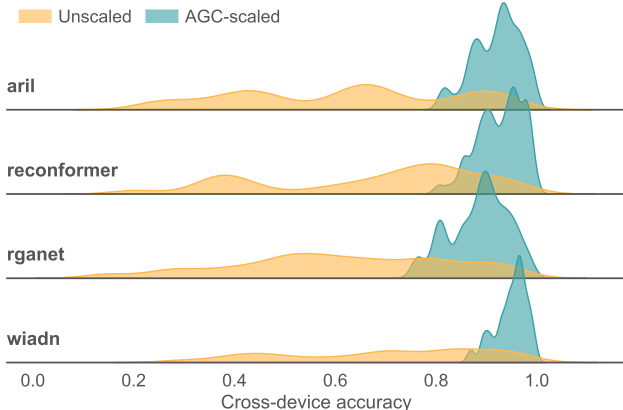


Figure 9. Distributions of cross-device accuracies for four HAR models before and after gain normalization, using feature-wise z-score standardization across examples. Curves aggregate off-diagonal accuracies across all train–test device pairs.

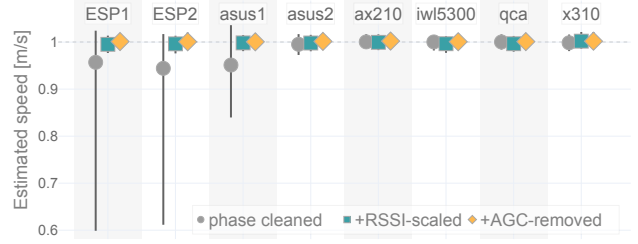


Figure 10. Median and IQR of Doppler-MUSIC velocity estimates under the three preprocessing schemes; the dashed line marks the ground-truth 1 m/s.

H. Doppler-based velocity estimation

Having shown that large-scale gain confounds the *learning* pipeline, we next test a *purely signal-processing-based* method. We use Doppler-MUSIC [6], [38], which estimates velocity from a CSI covariance matrix across packets and assumes that the signal statistics within each window are stable. Packet-to-packet gain changes from AGC break this assumption and should affect its estimates. To expose this effect clearly, we design a simple Doppler experiment with a single, perfectly known target velocity.

Synthetic ground truth: In real human motion, the measured Doppler is a superposition of reflections from multiple body parts. Even if a dominant component can often be isolated, its true velocity is not known, so we cannot quantify absolute error or bias against ground truth. We therefore emulate motion at the transmitter via packet-wise precoding $c_k(t) = a + b \cdot \exp(-j2\pi \frac{f_k \Delta(t)}{c})$, with f_k the subcarrier frequency, c the speed of light and $\Delta(t) = vt$ chosen to realize a constant velocity $v = 1$ m/s. Receivers then observe a synthetic two-path channel

$$\hat{H}_k(t) = \underbrace{a \cdot H_k^S}_{H_k^0} + \underbrace{b \cdot H_k^S \cdot \exp(-j2\pi \frac{f_k \Delta(t)}{c})}_{H_k^1(t)},$$

in which $a = 0.7$ and $b = 0.3$ fix the static-to-dynamic ratio. The linear growth of $\Delta(t)$ gives a perfectly constant Doppler shift, so the true velocity is known exactly and we can directly measure estimator bias and spread.

Data collection and processing: We collect data at 500 packets per second over 50 seconds and apply Doppler-MUSIC to windows of 50 CSI samples, using reported timestamps to estimate the effective gap time when packets are missing. For each packet, we remove a least-squares (LS) linear phase fit across subcarriers to correct the linear terms in Equation (2), which capture phase errors such as CFO; Section A considers an alternative using edge-subcarriers only to estimate slope. We always apply phase cleaning and then add either RSSI-based rescaling (Equation (3)) or large-scale-gain removal (Equation (4)).

Results: Figure 10 shows that, with AGC intact, velocity estimates from the two ESP32 units and *asus1* become *highly unstable*: their IQRs widen to up to 0.6 m/s, and their medians undershoot the 1 m/s ground truth by ≈ 4 cm/s. The second ASUS router (*asus2*) is almost unbiased, highlighting how device-internal AGC settings can *differ even within a product line*. Applying RSSI-based rescaling (Equation (3)) *collapses the spreads* and *removes the large positive bias* in all three

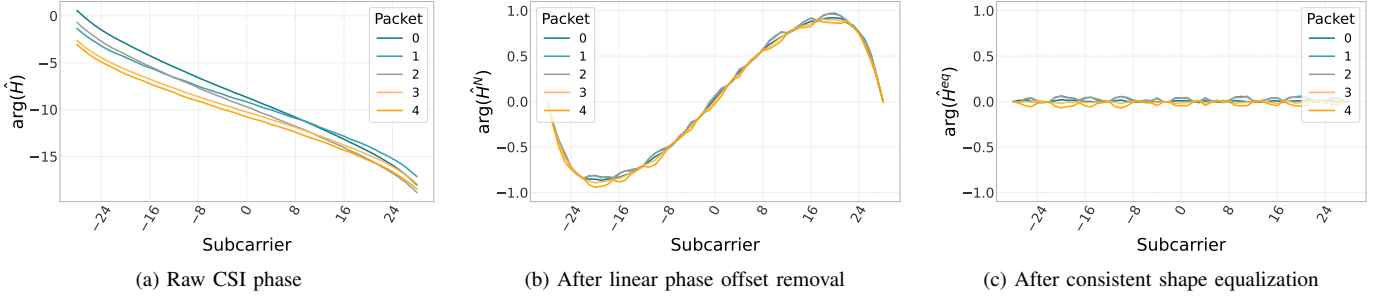


Figure 11. CSI preprocessing steps illustrated with *asus2*: (a) raw CSI phase, (b) after linear phase offset removal, and (c) after consistent shape equalization.

outliers, although a small negative offset persists in some medians. Eliminating large-scale gain *cures both problems*: all medians now lie within 2 mm/s of the target.

Why time-invariant distortions are harmless to MUSIC:

The time-invariant distortions investigated in Section V are unimportant to this method. A deterministic, packet-constant distortion is a fixed diagonal weight W , yielding $Y = XW$. Its sample covariance is $R_Y = YY^H = X(WW^H)X^H$, which rescales eigenvalues but leaves the signal and noise subspaces, and hence the MUSIC spectrum, unchanged. Doppler-MUSIC is therefore immune to any distortion that *stays fixed across packets*.

Take-away: AGC makes Doppler-MUSIC velocity estimates highly unstable. RSSI-based rescaling removes most spread but leaves a *small, systematic bias*, and is *outperformed by large-scale-gain removal* that also rescued the ML pipeline. Large-scale gain is thus anything but irrelevant to Doppler-MUSIC; erratic gain control is harmful yet straightforward to eliminate.

V. NONLINEAR DISTORTIONS

Beyond AGC-driven global amplitude scaling and random linear phase offsets, receiver hardware introduces subcarrier-dependent nonlinear distortions. As described in Section II-A, these effects, captured by the static terms A_k and Φ_k in Equation (2), persist even after correcting for global gain and linear phase offsets. Prior studies (π -Splicer [14], PicoScenes [15]) observed these distortions on few devices, but did not systematically verify time invariance or impact on downstream sensing across diverse receiver types.

To characterize these subcarrier-specific nonlinearities, we collect CSI from repeated transmissions of an unmodified packet in a fully static, cable-connected setup (no precoding). For each receiver, we then apply three preprocessing steps (Figure 11)

Phase correction: We unwrap phase across subcarriers and remove random linear phase offsets (see Equation 2) by subtracting a line fitted between the first and last subcarriers, following PADS [3]:

$$a = \frac{\arg(\hat{H}_K) - \arg(\hat{H}_0)}{m_K - m_0}, \quad b = \arg(\hat{H}_0),$$

where m_0 and m_K are indices of the first and last subcarriers. Using only the edge tones defines a fixed phase reference independent of the interior subcarriers, so that subcarrier-dependent distortions from precoding and hardware remain visible in the corrected CSI.

Amplitude correction: Next, we remove AGC-induced amplitude scaling by normalizing each packet per Equation (4). Remaining amplitude variations then reflect subcarrier-dependent nonlinearities on a shared scale.

Profile computation: Finally, we compute amplitude and phase profiles by averaging the normalized, phase-corrected CSI over N packets:

$$\bar{A}_k = \frac{1}{N} \sum_{n=1}^N |\hat{H}_{k,n}^N|, \quad \bar{\Phi}_k = \frac{1}{N} \sum_{n=1}^N \arg(\hat{H}_{k,n}^N), \quad (5)$$

resulting in the baseline channel profile

$$\bar{H}_k = \bar{A}_k e^{j\bar{\Phi}_k}. \quad (6)$$

These static profiles \bar{H}_k represent device-specific nonlinear distortions remaining after global corrections and serve as calibration references. In particular, we can equalize via

$$H^{eq} = \frac{\hat{H}}{\bar{H}}. \quad (7)$$

A. Consistency of distortions

The extended distortion model in Equation (2) assumes that the device-specific nonlinear distortions \bar{H}_k are time-invariant. We test this by repeating the profile extraction on five separate days under nominally identical laboratory conditions: on each day, we collect CSI from 10 000 repetitions of an unmodified packet, compute normalized channel profiles from Equation (6), and then compare them across days.

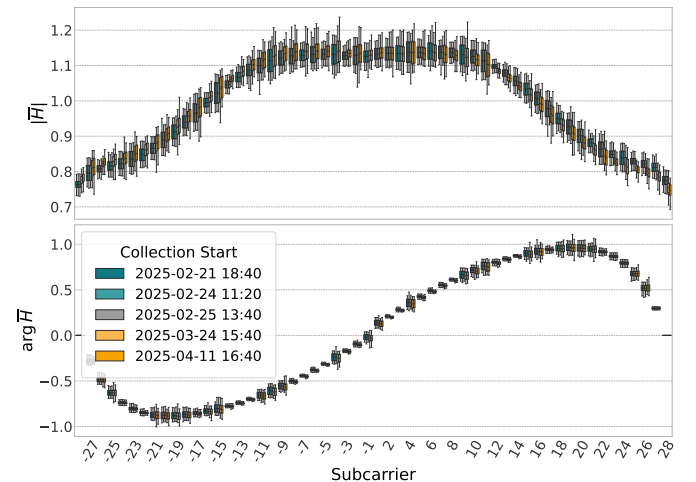


Figure 12. Nonlinear distortion boxplots for *asus1* measured on five distinct days.

Table I
STABILITY SCORES FOR ALL RECEIVERS.

| Receiver | Stability Score (S) |
|------------------|-------------------------|
| x310 (SDR) | 0.99998 |
| ax210 (Intel) | 0.99970 |
| iw15300 (Intel) | 0.99966 |
| qca (Qualcomm) | 0.99997 |
| asus1 (Broadcom) | 0.99994 |
| asus2 (Broadcom) | 0.99997 |
| ESP1 (Espressif) | 0.99993 |
| ESP2 (Espressif) | 0.99993 |

Figure 12 illustrates this for *asus1*: amplitude and phase medians, IQRs, and extremes almost coincide across days, indicating highly stable distortions. For brevity, we omit the other devices and instead summarize stability using cosine similarities between profiles from days i and j , $S_{ij} = \frac{\langle \overline{H}^{(i)}, \overline{H}^{(j)} \rangle}{|\overline{H}^{(i)}| |\overline{H}^{(j)}|}$, where $\overline{H}^{(i)}$ is the day- i profile. For each device we report the geometric mean $S = \left(\prod_{i < j} S_{ij} \right)^{2/(n(n-1))}$ over all day pairs, with n the number of measurement days. This score equals one only if all profiles are identical, and values close to one reflect strong day-to-day consistency. Stability scores for all receivers are given in Table I.

All devices achieve high stability scores, showing that the subcarrier-dependent nonlinear distortions are effectively static over days. This supports the static-distortion assumption in Equation (2) and justifies treating the extracted profiles as fixed calibration terms in subsequent experiments.

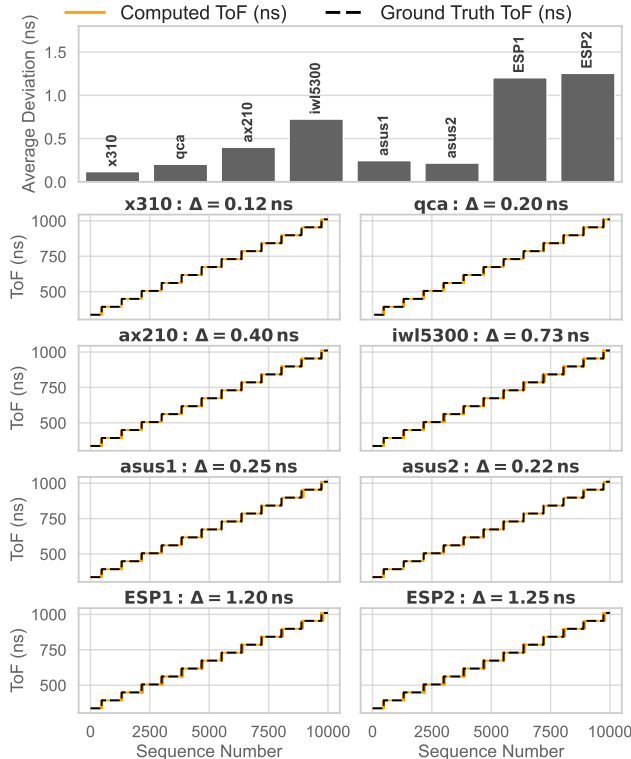


Figure 13. Time of flight estimates from PDP and ground truth over time.



Figure 14. ToF deviation from ground truth with and without nonlinearity equalization.

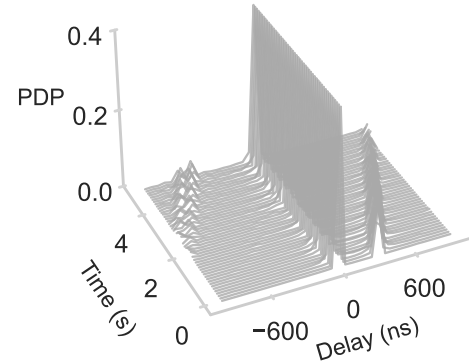


Figure 15. PDP of *iw15300* over time; truncated to 0.4 for visualization purposes.

B. PDP-based ToF estimation

Subcarrier nonlinearities also affect PDP-based ToF estimation. We compute the PDP as $\text{PDP}(\tau) = \left| \mathcal{F}^{-1}\{\hat{H}\}(\tau) \right|^2$, and again remove linear phase offsets with a LS fit (see Section A for a comparison with PADS). Because the DC subcarrier is absent in CSI while the Fast Fourier Transform (FFT) requires equally spaced frequency samples, we reconstruct the DC term by linear interpolation and then estimate ToF from prominent PDP peaks [13]. Specifically, we detect the two strongest peaks, take their positive delay difference as the path delay, and tune the peak-detection threshold separately for each device.

For accurate evaluation, we reuse the precoding scheme from Section IV-H, now letting $\Delta(t)$ increase linearly from 100 to 300 m over 50 s to induce a known ToF variation. We measure performance as the deviation between estimated ToF and ground truth (Figure 13). Because each device's bandwidth B limits its delay resolution to steps of $1/B$, estimates show a step-like behavior.

Nonlinear distortions substantially reshape the PDP. Figure 14 shows that equalizing them with Equation (7) clearly improves mean ToF accuracy and volatility across all devices. Among the tested receivers, *x310* and *qca* achieve the best accuracy, followed by Intel NICs, while *ASUS* routers gain the most from equalization.

To isolate the effect of reduced effective bandwidth, we show the PDP for Intel *iw15300* in Figure 15; other devices do not exhibit this artifact. *iw15300* reports CSI for only 30 subcarriers, effectively doubling the subcarrier spacing and introducing aliasing near 1600 ns. This yields prominent negative-delay peaks (a ToF ambiguity artifact) and degrades peak resolution at higher delays.

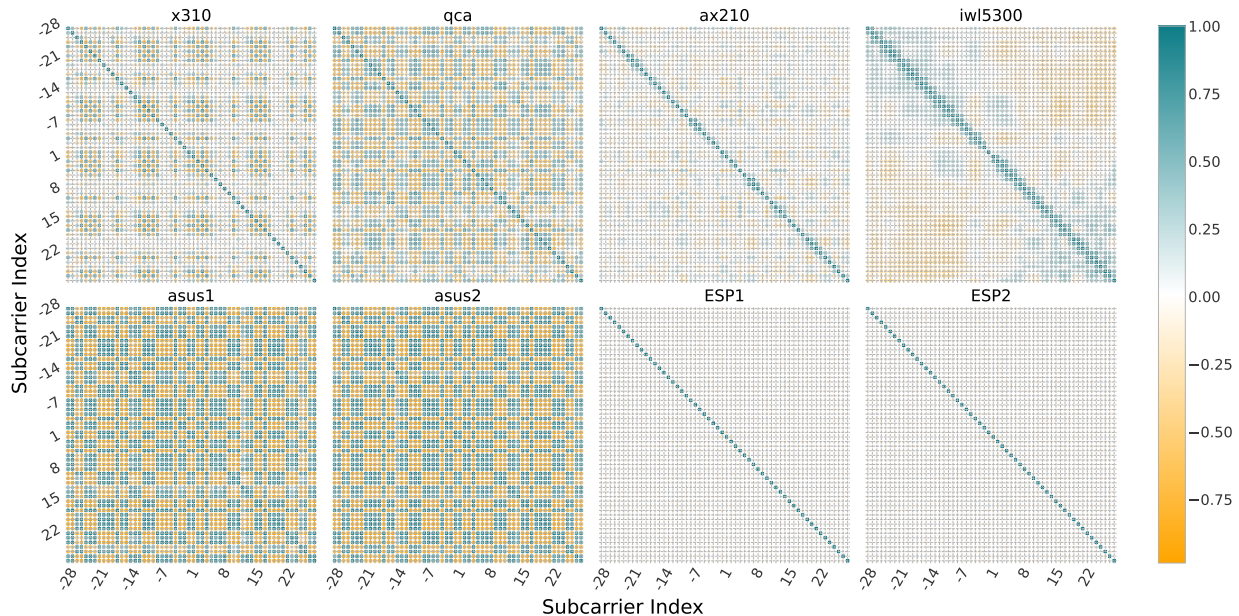


Figure 16. Static-environment correlation of \hat{H}' between different subcarriers for all receivers.

VI. BEYOND TRACTABLE DISTORTIONS

Our focus so far has been on distortions that are, at least in theory, predictable and correctable. However, CSI measurements are also inherently noisy, and their accuracy is limited by hardware-specific constraints and imperfections in the estimation algorithm.

We now probe noise, faithfulness, and sensitivity of the estimator E , beyond Equation (2). We selectively precode a subset of subcarriers to isolate localized effects against a shared baseline. Preprocessing follows Section V except that precoded tones are excluded from the gain calculation, anchoring unmodified tones. Concretely, $\hat{H}_k^N = \frac{\hat{H}_k}{\sum_{u \in U} |\hat{H}_u|}$, where U denotes the set of non-precoded subcarriers. This removes the effects in Equation (2); remaining differences between precoded and unmodified tones reflect estimation error or residual, non-modeled distortions.

A. Noise characteristics

We analyze equalized CSI H^{eq} from 10 000 repetitions of an unmodified packet under controlled conditions. We chose per-subcarrier metrics SD, IQR, skewness, and excess kurtosis. Because these ignore cross-tone dependencies, we also quantify

cross-subcarrier noise correlations (sometimes assumed zero; e.g., [9], [39]), which may accumulate when averaging across tones and have not been systematically examined.

1) *Amplitude Noise*: We analyze amplitude noise by computing the above metrics per subcarrier and then averaging across subcarriers. Table II summarizes results per receiver. The *x310* (SDR) shows the lowest noise (lowest SD and IQR). Among COTS devices, the *ax210* (Intel) stands out with a particularly low SD, likely benefiting from internal subcarrier smoothing (see Section VI-C). The *iwl5300* (Intel), *qca* (Qualcomm), and *ESP32* (Espressif) exhibit near-normal amplitude noise (skewness and excess kurtosis close to zero). In contrast, *asus1* and *asus2* (Broadcom) show extremely high kurtosis (> 40), not as precise values but as indicators of rare, severe outliers; for example, removing around 20 Mahalanobis-distance outliers on *asus1* reduces kurtosis from 43.259 to 0.82, with a similar improvement for *asus2*. This underscores the value of reporting skewness and kurtosis alongside SD and IQR, which can hide such outlier behavior.

2) *Phase Noise*: We perform the same analysis for phase noise. Table III summarizes metrics per receiver. Consistent with the amplitude results, the *x310* shows the lowest variability, followed by the *ax210*. The *iwl5300* (Intel), *qca*

Table II

AMPLITUDE NOISE METRICS FOR DIFFERENT RECEIVERS, SUMMARIZING STANDARD DEVIATION (SD), IQR, SKEWNESS, AND KURTOSIS.

| Receiver | SD | IQR | Skewness | Kurtosis |
|------------------|-------|-------|----------|----------|
| x310 (SDR) | 0.003 | 0.004 | 0.006 | 0.148 |
| ax210 (Intel) | 0.004 | 0.006 | 0.147 | 0.444 |
| iwl5300 (Intel) | 0.013 | 0.018 | -0.049 | -0.277 |
| qca (Qualcomm) | 0.015 | 0.023 | 0.005 | -0.525 |
| asus1 (Broadcom) | 0.015 | 0.026 | -0.450 | 43.259 |
| asus2 (Broadcom) | 0.017 | 0.031 | -0.285 | 17.710 |
| ESP1 (Espressif) | 0.035 | 0.048 | -0.005 | -0.016 |
| ESP2 (Espressif) | 0.037 | 0.050 | 0.003 | -0.002 |

Table III

PHASE NOISE METRICS FOR DIFFERENT RECEIVERS, SUMMARIZING SD, IQR, SKEWNESS, AND KURTOSIS.

| Receiver | SD | IQR | Skewness | Kurtosis |
|------------------|-------|-------|----------|----------|
| x310 (SDR) | 0.004 | 0.005 | -0.013 | 0.405 |
| ax210 (Intel) | 0.007 | 0.009 | -0.046 | 0.117 |
| iwl5300 (Intel) | 0.018 | 0.025 | -0.030 | -0.203 |
| qca (Qualcomm) | 0.018 | 0.028 | 0.110 | 0.219 |
| asus1 (Broadcom) | 0.020 | 0.032 | 1.968 | 87.702 |
| asus2 (Broadcom) | 0.020 | 0.036 | 2.832 | 176.879 |
| ESP1 (Espressif) | 0.049 | 0.066 | 0.002 | 0.319 |
| ESP2 (Espressif) | 0.052 | 0.070 | 0.002 | 0.288 |

(Qualcomm), and *ESP32* (Espressif) exhibit near-normal phase noise (skewness and kurtosis close to zero), whereas *asus1* and *asus2* (Broadcom) show extreme phase kurtosis, indicating rare but large outliers. When outliers identified by *amplitude* deviations are removed, both skewness and kurtosis return to levels comparable to the other NICs, corroborating that these samples are invalid CSI.

3) *Noise Correlation*: We further examine noise correlation across subcarriers. Figure 16 shows that *ESP32* microcontrollers, despite higher per-subcarrier noise power, exhibit minimal cross-subcarrier correlation. In contrast, the *ASUS* routers and the *qca* NIC show strong cross-subcarrier correlations with near-identical patterns, suggesting a shared hardware component (e.g., a filtering stage).

Overall, while receivers differ in noise characteristics, all maintain *low* absolute noise. Cross-subcarrier correlations, particularly in the *ASUS* routers, introduce an additional factor that *may influence downstream performance*. *High-fidelity* applications may favor the *x310*, and users of *ASUS* devices should consider mitigation strategies for rare strong outliers. Ultimately, receiver choice depends on an application’s tolerance for noise magnitude, correlation, and outlier events.

B. Faithfulness

Accurate channel estimation is *fundamental* for the reliability of CSI-based applications. A *strong alignment* between the estimated channel and the actual channel ensures that signal processing methods, which often rely on *precise channel models*, function as intended. *Discrepancies* between the estimated and true channel can *violate these core assumptions*, undermining the effectiveness of downstream applications.

To quantify this alignment, we introduce the concept of **faithfulness**, which measures how closely the channel estimate mirrors the actual channel characteristics. Specifically, we define the **mean phase and amplitude response deviations** as follows:

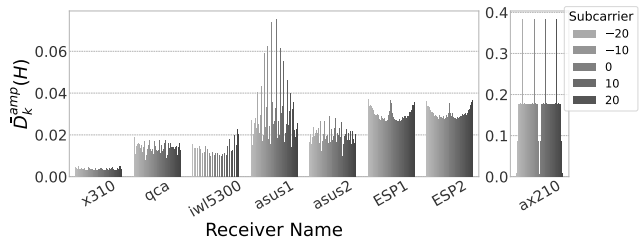
$$\bar{D}_k^{amp}(H) = \frac{1}{N} \sum_{n=1}^N \left| |H_{k,n}^{eq}| - |c_n| \right|,$$

$$\bar{D}_k^{phs}(H) = \frac{1}{N} \sum_{n=1}^N \left| \arg(H_{k,n}^{eq}) - \arg(c_n) \right|,$$

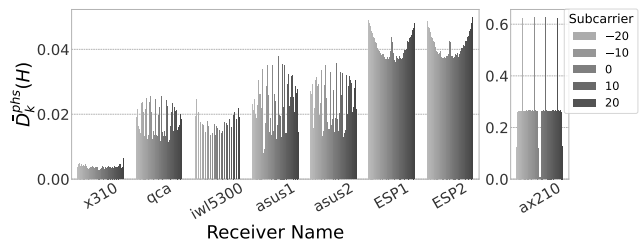
where c_n is the introduced complex precoding factor in the n -th out of a total of N packets and $\hat{H}'_{n,k}$ the corresponding detected and equalized CSI on subcarrier k .

We use $N = 1000$ packets and vary precoding amplitudes equidistantly between $[0, 2]$, and phases between $[0, \frac{\pi}{2}]$.

The results in Figure 17a and Figure 17b highlight notable differences in faithfulness across devices. With the exception of the *ax210*, all devices demonstrate high faithfulness, albeit with some variation. As expected due to its premium build quality, the *x310* boasts both the least overall deviations as well as the highest consistency across subcarriers. For the others, a pronounced subcarrier dependency is evident. *ASUS* devices and *qca* exhibit larger deviations on a non-systematic set of subcarriers, especially pronounced in phase. The *ESP32*s, on the other hand, show a clear shape, with



(a) Mean amplitude response deviation.



(b) Mean phase response deviation

Figure 17. Mean response deviations for all devices and subcarriers.

slightly larger deviations towards edge and DC subcarriers. Notably, there is a strong difference between the two *ASUS* routers, confirming that even devices of the same family can vary strongly. The *iw5300* performs remarkably well, given its age, showcasing only a slight dependence on frequency and a comparatively low mean phase response deviation. The *ax210* stands out as an outlier, exhibiting significant deviations in both amplitude and phase. We examine these anomalies further in Section VI-C.

Notably, the order of average deviation closely aligns with the ranking in accuracies observed in Section V-B, confirming that *device capabilities are distinct in high-precision tasks*.

C. Intel ax210 smoothing

The large deviation from the expected scaling on individual subcarriers observed in the Intel *ax210* CSI measurements stems from a smoothing mechanism implemented by the device. To demonstrate this, we apply a magnitude precoding factor of 2 across a larger block of subcarriers.

Figure 18 compares the reported CSI from the *ax210* to that of the *x310*. In the center of the block, both devices detect the correct scaling. However, the *ax210* exhibits a consistent smoothing effect at the block edges, suggesting an internal averaging process. Notably, this smoothing also affects phase measurements, even though phase values remain unaltered by the applied precoding. A similar smoothing effect is observed when applying phase precoding across a block of subcarriers.

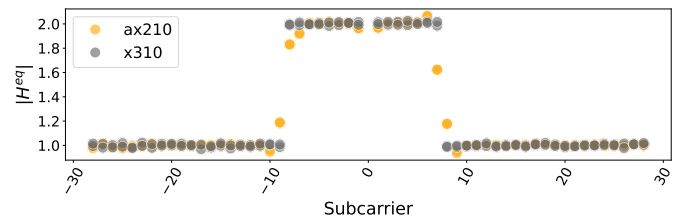


Figure 18. Detected magnitude scaling after precoding a block of subcarriers by a factor of 2.

While this may be relevant for applications with a narrow coherence bandwidth, we could not observe any negative impact in any of our tests, as demonstrated in the presented applications. Neither PDP, Doppler velocity, nor neural networks manifest in a measurable negative performance hit for the *ax210*.

D. Sensitivity

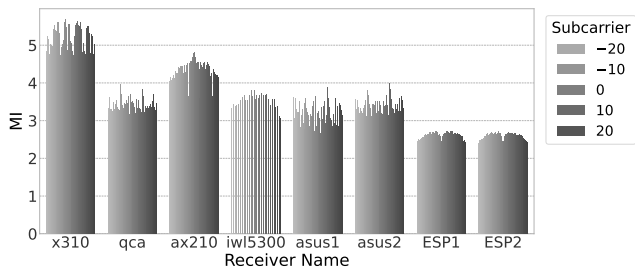
Neural networks have changed the rules for CSI-based applications: *fidelity no longer defines data quality; exploitable structure does*. What matters is whether the data moves with the channel in a *consistent, learnable pattern*. If it does, neural networks can extract meaningful insights. If it does not, *no procedure, no matter how powerful, can uncover what is not there*.

To reveal how much exploitable structure each device provides, we measure the *sensitivity* to the controlled channel variations c_k in the reported estimates \hat{H}'_k with Mutual Information (MI), $I(c_k; \hat{H}'_k)$. MI answers the precise question we care about: *how much information about the channel does the CSI reveal?* Formally,

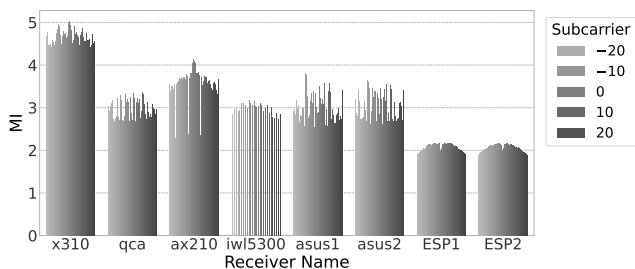
$$I(c_k; \hat{H}'_k) = \iint p_{c, \hat{H}'_k}(c_k, \hat{H}'_k) \ln \frac{p_{c, \hat{H}'_k}(c_k, \hat{H}'_k)}{p_c(c_k) p_{\hat{H}'_k}(\hat{H}'_k)} dc_k d\hat{H}'_k,$$

where p_{c, \hat{H}'_k} is the joint density and $p_c, p_{\hat{H}'_k}$ the marginals. The logarithm is natural, so I is in *nats*. A value of $I = 0$ implies statistical independence; larger values indicate stronger dependence and greater potential for downstream procedures to distinguish channel variations.

We estimate I with the k -nearest-neighbor method of Kraskov [40].



(a) Average amplitude sensitivity.



(b) Average phase sensitivity.

Figure 19. Average sensitivity for all devices and subcarriers, quantified with mutual information. Larger values indicate stronger coupling between channel variations and reported estimates.

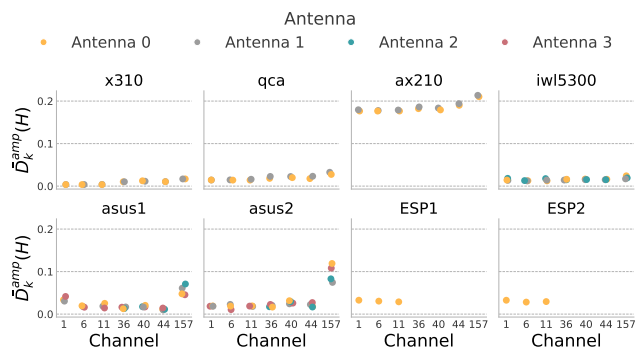
Results: The MI mirrors the faithfulness analysis in Section VI-B (Figure 19). We again see the *x310* leading by a significant margin. The *ax210*'s averaging is irrelevant for MI; it shows the second-highest values across subcarriers, with slight dips on pilots. *qca* and *iw15300* perform similarly, strong despite their age, and on levels comparable to the *ASUS* routers. While *asus1* appears slightly worse than its twin, the difference does not seem significant. The *ESP32*s bring up the rear, behaving similarly and showing a small nudge around DC.

All devices yield MI well above zero, confirming that each subcarrier conveys substantial information about the underlying channel. Absolute gaps are relatively small, suggesting that despite architectural differences, every device captures a similarly large amount of exploitable structure. We therefore expect similar performance on coarse-grained tasks, with *subtle MI differences* influencing only applications demanding high precision, as in Section V-B.

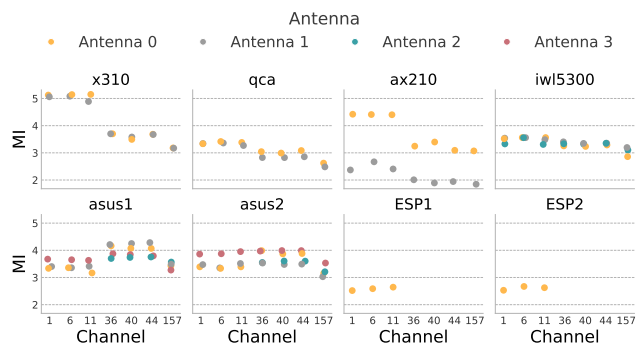
E. Channel, band and antenna dependence

We next investigate how faithfulness and sensitivity depend on wireless channel and receive chain. For each device, we repeat the experiment across multiple channels, capturing an identical signal simultaneously on all receive chains. For clarity, we report the subcarrier median.

The results in Figure 20a and Figure 20b show minimal variation across most channels and chains. *ASUS* routers exhibit a clear systematic deviation of faithfulness in channel 157—their reported values consistently differ from expectation. Crucially,



(a) Amplitude response deviation. Lower is better.



(b) Amplitude sensitivity. Higher is better.

Figure 20. Median (across subcarriers) mean (across time) amplitude response deviation and sensitivities for different channels (1, 6, 11 in 2.4 GHz, 36, 40, 44, 157 in 5 GHz bands) and antennas.

sensitivity does not drop, indicating a systematic (informationally irrelevant) offset rather than signal degradation.

In contrast, *x310* and *ax210* show a marked sensitivity decrease on the 5 GHz channels (36, 40, 44, 157), *qca* shows a slight reduction, and other devices remain stable. Antenna-wise, *ASUS* devices show selective chain differences by channel. Most notably, the two *ax210* receive chains diverge sharply, with the second underperforming; the *ax210* labels its antennas *primary* and *secondary*, possibly suggesting differing capabilities.

Although channel- and antenna-dependent effects are subtle, they matter for interpreting measurements. Despite reduced high-channel sensitivity, *x310* remains superior or on par overall. Phase sensitivity and faithfulness show the same qualitative trends (omitted for brevity).

VII. CONCLUSION

In this work, we systematically investigated the impact of receiver-specific effects on Wi-Fi CSI across a wide range of off-the-shelf hardware platforms. Using a combination of controlled cable-coupled experiments with precisely engineered precoded signals and OTA evaluations, we successfully disentangled receiver-induced artifacts from inherent wireless channel characteristics. Our OTA experiments specifically demonstrated how hardware-dependent differences, primarily driven by AGC, impose substantial variability that severely limits cross-device portability of sensing models.

Collectively, our insights lead to a practical, hardware-agnostic preprocessing pipeline: acquiring raw CSI, applying ℓ_1 gain removal with feature-wise standardization, and calibrating stable subcarrier nonlinearities. Validated across four human activity recognition architectures and against a range of existing gain preprocessing and standardization schemes, this pipeline significantly enhances device agnosticism and supports practical, robust, and portable Wi-Fi sensing deployments.

Future Work: To further enhance hardware independence, future work should explore adaptive, self-supervised preprocessing capable of mitigating receiver-specific distortions in situ. Eliminating reference cables through cable-free calibration could also streamline deployment.

Even marginal improvements in recovering large-scale gain shifts would advance plug-and-play sensing. Standardizing CSI reporting, e.g., normalized value ranges and explicit AGC reporting, in the IEEE 802.11bf amendment would promote robust, cross-device interoperability.

Another open question is how individual hardware aspects, for example effective CSI bits, dynamic range limits, and filter responses, each shape the observed mismatch between receivers. If these contributions can be quantified, basic hardware descriptors might be sufficient to design informed rules for transferring models across devices.

DATA AND CODE AVAILABILITY

Our CSI measurements, derived data, and the full collection and processing pipeline used in this paper are publicly available. The datasets, containing HAR and over-the-cable data,

as well as resulting figures, are archived at <https://doi.org/10.4121/48e1331b-91df-4e1a-906b-b0a0e9d16c74>, and the collection, neural network training and processing scripts are available at <https://github.com/nzqo/senssession>.

VIII. ACKNOWLEDGMENT

This research has been partially funded by the European Union's EU Framework Programme for Research and Innovation under the HORIZON-MSCA-DN-2022 Grant Agreement No. 101119652 (MSCA-DN-6th Sense). This work has been partially supported by DFG SenShield (447586980) and partially funded by the LOEWE initiative (Hesse, Germany) within the emergenCITY center [LOEWE/1/12/519/03/05.001(0016)/72]. This work was further partially supported by the European Union - Next Generation EU under the Italian National Recovery and Resilience Plan (NRRP), Mission 4, Component 2, Investment 1.3, CUP E63C22002070006, partnership on "Telecommunications of the Future" (PE00000001 - program "RESTART").

REFERENCES

- [1] V. V. Ratnam, H. Chen, H.-H. Chang, A. Sehgal, and J. Zhang, "Optimal preprocessing of wifi csi for sensing applications," *IEEE Transactions on Wireless Communications*, vol. 23, no. 9, pp. 10820–10833, 2024.
- [2] X. Niu, S. Li, Y. Zhang, Z. Liu, D. Wu, R. C. Shah, C. Tanriover, H. Lu, and D. Zhang, "Wimonitor: Continuous long-term human vitality monitoring using commodity wi-fi devices," *Sensors*, vol. 21, no. 3, p. 751, 2021.
- [3] K. Qian, C. Wu, Z. Yang, Y. Liu, and Z. Zhou, "Pads: Passive detection of moving targets with dynamic speed using phy layer information," in *2014 20th IEEE International Conference on Parallel and Distributed Systems (ICPADS)*. Piscataway, NJ, USA: IEEE, 2014, pp. 1–8.
- [4] A. Zubow, P. Gawłowicz, and F. Dressler, "On phase offsets of 802.11 ac commodity wifi," in *2021 16th Annual Conference on Wireless On-demand Network Systems and Services (WONS)*, IEEE. Klosters, Switzerland: IEEE, 2021, pp. 1–4.
- [5] D. Zhang, Y. Hu, Y. Chen, and B. Zeng, "Calibrating phase offsets for commodity wifi," *IEEE Systems Journal*, vol. 14, no. 1, pp. 661–664, 2019.
- [6] X. Li, D. Zhang, Q. Lv, J. Xiong, S. Li, Y. Zhang, and H. Mei, "Indotrack: Device-free indoor human tracking with commodity wi-fi," *Proceedings of the ACM on Interactive, Mobile, Wearable and Ubiquitous Technologies*, vol. 1, no. 3, pp. 1–22, 2017.
- [7] G. Chi, Z. Yang, J. Xu, C. Wu, J. Zhang, J. Liang, and Y. Liu, "Wi-drone: wi-fi-based 6-dof tracking for indoor drone flight control," in *Proceedings of the 20th Annual International Conference on Mobile Systems, Applications and Services*, ser. MobiSys '22. New York, NY, USA: Association for Computing Machinery, 2022, p. 56–68. [Online]. Available: <https://doi.org/10.1145/3498361.3538936>
- [8] Y. Chen, X. Su, Y. Hu, and B. Zeng, "Residual carrier frequency offset estimation and compensation for commodity wifi," *IEEE Transactions on Mobile Computing*, vol. 19, no. 12, pp. 2891–2902, 2019.
- [9] H. Vogt, C. Li, A. Sezgin, and C. Zenger, "On the precise phase recovery for physical-layer authentication in dynamic channels," in *2019 IEEE International Workshop on Information Forensics and Security (WIFS)*. Piscataway, NJ, USA: IEEE, 2019, pp. 1–6.
- [10] N. Tadayon, M. T. Rahman, S. Han, S. Valaee, and W. Yu, "Decimeter ranging with channel state information," *IEEE Transactions on Wireless Communications*, vol. 18, no. 7, pp. 3453–3468, 2019.
- [11] E. Yi, F. Zhang, J. Xiong, K. Niu, Z. Yao, and D. Zhang, "Enabling wifi sensing on new-generation wifi cards," *Proceedings of the ACM on Interactive, Mobile, Wearable and Ubiquitous Technologies*, vol. 7, no. 4, Jan. 2024. [Online]. Available: <https://doi.org/10.1145/3633807>
- [12] C. Li, J. Brauer, A. Sezgin, and C. Zenger, "Kalman filter based mimo csi phase recovery for cots wifi devices," in *ICASSP 2021 - 2021 IEEE International Conference on Acoustics, Speech and Signal Processing (ICASSP)*. 2711 Pierre Place, College Station, Texas 77845, USA: IEEE, 2021, pp. 4820–4824.

- [13] Y. Xie, Z. Li, and M. Li, "Precise power delay profiling with commodity wifi," in *Proceedings of the 21st Annual International Conference on Mobile Computing and Networking*, ser. MobiCom '15. New York, NY, USA: ACM, 2015, p. 53–64. [Online]. Available: <http://doi.acm.org/10.1145/2789168.2790124>
- [14] H. Zhu, Y. Zhuo, Q. Liu, and S. Chang, " π -splicer: Perceiving accurate csi phases with commodity wifi devices," *IEEE Transactions on Mobile Computing*, vol. 17, no. 9, pp. 2155–2165, 2018.
- [15] Z. Jiang, T. H. Luan, X. Ren, D. Lv, H. Hao, J. Wang, K. Zhao, W. Xi, Y. Xu, and R. Li, "Eliminating the barriers: Demystifying wi-fi baseband design and introducing the picoscenes wi-fi sensing platform," *IEEE Internet of Things Journal*, vol. 9, no. 6, pp. 4476–4496, 2021.
- [16] D. Halperin, W. Hu, A. Sheth, and D. Wetherall, "Tool release: Gathering 802.11n traces with channel state information," *ACM SIGCOMM CCR*, vol. 41, no. 1, p. 53, Jan. 2011.
- [17] S. M. Hernandez and E. Bulut, "Lightweight and Standalone IoT Based WiFi Sensing for Active Repositioning and Mobility," in *2020 IEEE 21st International Symposium on "A World of Wireless, Mobile and Multimedia Networks" (WoWMoM)*. Los Alamitos, CA, USA: IEEE Computer Society, Sep. 2020, pp. 277–286. [Online]. Available: <https://doi.ieeecomputersociety.org/10.1109/WoWMoM49955.2020.00056>
- [18] D. Tse and P. Viswanath, *Fundamentals of wireless communication*. USA: Cambridge University Press, 2005.
- [19] K. Wu, J. Pegoraro, F. Meneghello, J. A. Zhang, J. O. Lacruz, J. Widmer, F. Restuccia, M. Rossi, X. Huang, D. Zhang, G. Caire, and Y. J. Guo, "Sensing in bistatic isac systems with clock asynchronism: A signal processing perspective," *IEEE Signal Processing Magazine*, vol. 41, no. 5, pp. 31–43, 2024.
- [20] F. Gringoli, M. Schulz, J. Link, and M. Hollick, "Free your csi: A channel state information extraction platform for modern wi-fi chipsets," in *Proceedings of the 13th International Workshop on Wireless Network Testbeds, Experimental Evaluation & Characterization*, ser. WiNTECH '19. New York, NY, USA: Association for Computing Machinery, 2019, p. 21–28. [Online]. Available: <https://doi.org/10.1145/3349623.3355477>
- [21] Y. Zhuo, H. Zhu, and H. Xue, "Identifying a new non-linear csi phase measurement error with commodity wifi devices," in *2016 IEEE 22nd International Conference on Parallel and Distributed Systems (ICPADS)*. Piscataway, NJ, USA: IEEE, 2016, pp. 72–79.
- [22] F. Wang, J. Feng, Y. Zhao, X. Zhang, S. Zhang, and J. Han, "Joint activity recognition and indoor localization with wifi fingerprints," *IEEE Access*, vol. 7, pp. 80058–80068, 2019.
- [23] I. Tsamardinos, "Don't lose samples to estimation," *Patterns*, vol. 3, no. 12, p. 100612, 2022. [Online]. Available: <https://www.sciencedirect.com/science/article/pii/S2666389922002379>
- [24] Y. Bengio and Y. Grandvalet, "No unbiased estimator of the variance of k-fold cross-validation," in *Advances in Neural Information Processing Systems*, S. Thrun, L. Saul, and B. Schölkopf, Eds., vol. 16. Cambridge, MA, USA: MIT Press, 2003. [Online]. Available: https://proceedings.neurips.cc/paper_files/paper/2003/file/e82c4b19b8151ddc25d4d93abf7b908f-Paper.pdf
- [25] J. Kim, "Estimating classification error rate: Repeated cross-validation, repeated hold-out and bootstrap," *Computational Statistics & Data Analysis*, vol. 53, no. 11, pp. 3735–3745, 2009. [Online]. Available: <https://www.sciencedirect.com/science/article/pii/S0167947309001601>
- [26] Z. Gao, Y. Gao, S. Wang, D. Li, and Y. Xu, "Crisloc: Reconstructable csi fingerprinting for indoor smartphoning localization," *IEEE Internet of Things Journal*, vol. 8, no. 5, pp. 3422–3437, 2020.
- [27] E. L. Lehmann and G. Casella, *Theory of Point Estimation*, 2nd ed., ser. Springer Texts in Statistics. New York, NY: Springer Science & Business Media, 2006, vol. 57.
- [28] B. Efron, "Better bootstrap confidence intervals," *Journal of the American Statistical Association*, vol. 82, no. 397, pp. 171–185, 1987. [Online]. Available: <http://www.jstor.org/stable/2289144>
- [29] J. M. Rocamora, I. W.-H. Ho, and M.-W. Mak, "Gaussian models for csi fingerprinting in practical indoor environment identification," in *Proceedings of the IEEE Global Communications Conference (GLOBECOM 2020)*. Piscataway, NJ, USA: Institute of Electrical and Electronics Engineers (IEEE), 2020, pp. 1–6.
- [30] C.-L. Chen, C.-H. Ko, S.-H. Wu, H.-S. Tseng, and R. Y. Chang, "Device-free target following with deep spatial and temporal structures of csi," *J. Signal Process. Syst.*, vol. 95, no. 11, p. 1327–1340, Jun. 2023. [Online]. Available: <https://doi.org/10.1007/s11265-023-01862-y>
- [31] J. Liu, Y. Zeng, T. Gu, L. Wang, and D. Zhang, "Wiphone: Smartphone-based respiration monitoring using ambient reflected wifi signals," *Proceedings of the ACM on Interactive, Mobile, Wearable and Ubiquitous Technologies*, vol. 5, no. 1, pp. 1–19, 2021.
- [32] J. Shang and J. Wu, "A robust sign language recognition system with multiple wi-fi devices," in *Proceedings of the Workshop on Mobility in the Evolving Internet Architecture*, ser. MobiArch '17. New York, NY, USA: Association for Computing Machinery, 2017, pp. 19–24. [Online]. Available: <https://doi.org/10.1145/3097620.3097624>
- [33] Y. Zeng, D. Wu, R. Gao, T. Gu, and D. Zhang, "Fullbreathe: Full human respiration detection exploiting complementarity of csi phase and amplitude of wifi signals," *Proceedings of the ACM on Interactive, Mobile, Wearable and Ubiquitous Technologies*, vol. 2, no. 3, pp. 1–19, 2018.
- [34] X. Liu, J. Cao, S. Tang, and J. Wen, "Wi-sleep: Contactless sleep monitoring via wifi signals," in *Proceedings of the 35th IEEE Real-Time Systems Symposium (RTSS)*. Piscataway, NJ, USA: IEEE Computer Society, 2014, pp. 346–355.
- [35] J. Zhou, X. Liao, Z. Gao, Q. Li, and C. Zheng, "Wiadn: Asymmetrical dual-task attention network for wifi sensing," *IEEE Internet of Things Journal*, vol. 11, no. 24, pp. 39435–39447, 2024.
- [36] M. Shang and X. Hong, "Recurrent conformer for wifi activity recognition," *IEEE/CAA Journal of Automatica Sinica*, vol. 10, no. 6, pp. 1491–1493, 2023.
- [37] J. Hu, F. Ge, X. Cao, and Z. Yang, "Rganet: A human activity recognition model for extracting temporal and spatial features from wifi channel state information," *Sensors*, no. 3, 2025. [Online]. Available: <https://www.mdpi.com/1424-8220/25/3/918>
- [38] M. Cominelli, S. Shahcheraghi, J. Link, M. Hollick, F. Cerutti, F. Gringoli, and A. Asadi, "Physical-layer privacy via randomized beamforming against adversarial wi-fi sensing: Analysis, implementation, and evaluation," *IEEE Transactions on Wireless Communications*, vol. 23, no. 12, pp. 19603–19617, 2024.
- [39] X. Wang, L. Gao, and S. Mao, "Csi phase fingerprinting for indoor localization with a deep learning approach," *IEEE Internet of Things Journal*, vol. 3, no. 6, pp. 1113–1123, 2016.
- [40] A. Kraskov, H. Stögbauer, and P. Grassberger, "Estimating mutual information," *Phys. Rev. E*, vol. 69, p. 066138, Jun 2004. [Online]. Available: <https://link.aps.org/doi/10.1103/PhysRevE.69.066138>

APPENDIX

A. Effect of phase sanitization methods

In Section IV-H, we remove linear phase ramps by subtracting a least-squares (LS) fit across subcarriers. An alternative, presented first in PADS [3], estimates the slope only from the outermost subcarriers and removes the offset as the mean. Here, we compare these two phase sanitization schemes across all receivers and tasks.

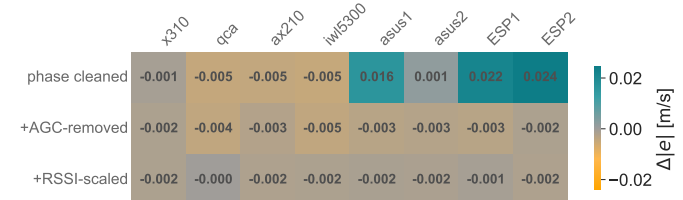


Figure 21. Change in Doppler velocity estimation error when using LS instead of PADS. Negative values indicate that LS yields lower error.

Figure 21 summarizes the impact of LS versus PADS phase sanitization on the Doppler-MUSIC velocity estimates. Each matrix entry shows the change in Doppler velocity estimation error when replacing PADS by LS for a given receiver and preprocessing variant (phase cleaned, Received Signal Strength Indicator (RSSI)-scaled, or Automatic Gain Control (AGC)-compensated data). Negative values indicate that LS yields lower error than PADS. Once large-scale gain effects have been handled (RSSI scaling or AGC compensation), the LS method consistently outperforms PADS on every receiver, typically reducing the Doppler error by about 1–5 mm/s.

On the data that was only phase-cleaned, without any large-scale gain correction, the difference between the two phase sanitization methods is less systematic.

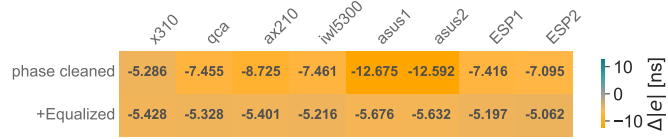


Figure 22. Change in ToF estimation error when using LS instead of PADS. Negative values indicate that LS yields lower error.

Figure 22 shows a similar comparison for the ToF estimates from Section V-B. Here, we consider phase-cleaned and shape-equalized data and report the change in ToF estimation error when switching from the PADS slope estimate to LS. With the PADS slope estimate on equalized data, all ToF errors stay on the order of 5–6 ns across receivers. Switching to the LS fit reduces these errors by approximately 5–5.7 ns, bringing the best receiver (x310) down to 0.12 ns and the NIC-class cards into the 0.2–0.7 ns range, with only the ESP boards still slightly above 1 ns. Thus, LS phase sanitization is an important enabler for the high absolute accuracies we report, while the remaining performance spread is still dominated by receiver-dependent effects.